Emerging co-synthesis of dimethyl oxalate and dimethyl carbonate using Pd/silicalite-1 catalyst with synergistic interactions of Pd and silanols

Chunzheng Wang, Ningkun Xu, Ke Huang, Bin Liu, Peihua Zhang, Ge Yang, Hailing Guo, Peng Bai, Svetlana Mintova

Emerging co-synthesis of dimethyl oxalate and dimethyl carbonate using Pd/silicalite-1 catalyst with synergistic interactions of Pd and silanols

Chunzheng Wang,[a,*] Ningkun Xu,[a] Ke Huang,[a] Bin Liu,[a] Peihua Zhang,[a] Ge Yang,[a] Hailing Guo,[a] Peng Bai,[a,*] and Svetlana Mintova,[a,b,*]

[a] *State Key Laboratory of Heavy Oil Processing, China University of Petroleum (East China), Qingdao 266580, China*

[b] *Normandie Université, Laboratoire Catalyse et Spectrochimie (LCS), ENSICAEN, UNICAEN, CNRS, 14050 Caen, France*

* Corresponding authors. E-mail addresses: czwang@upc.edu.cn (C. Wang), baipeng@upc.edu.cn (P. Bai), svetlana.mintova@ensicaen.fr (S. Mintova)

Abstract

An emerging synthetic route for the co-synthesis of dimethyl oxalate (DMO) and dimethyl carbonate (DMC) via the indirect oxidative carbonylation of CH_3OH is presented. The promising co-synthesis process combines the advantages of two separate routes of DMO and DMC syntheses. Herein, palladium containing silicalite-1 zeolite (Pd/S-1) catalyst was first found to be highly active and stable for the

co-synthesis of DMO and DMC. The catalytic performance strongly depended on the catalyst activation, as the heat treatment could tune the silanols around the Pd species on the silicalite-1 zeolite. The Pd/S-1 catalyst with abundant silanols exhibited a higher turnover frequency (TOF) of 0.18 s^{-1} and a lower apparent activation energy of 51 kJ mol^{-1} in comparison to the catalyst with low silanol sites (0.06 s^{-1} and 101 kJ mol^{-1}). The best performing catalyst had an average Pd nanoparticle size of 3.2 nm and Pd loading of 0.48 wt%. This catalyst showed a high CO conversion of 78% and DMO+DMC selectivity of 96%, maintaining high stability for at least 200 h. Furthermore, the synergistic interactions of silanols of silicalite-1 zeolite and Pd were confirmed by a series of in situ infrared experiments, and were found to be responsible for the enhanced activity. The silanols of S-1 zeolite played an essential role in forming the Pd active sites and had a very pronounced effect on the adsorption of CO reactant on the Pd species. Understanding the interactions between metal species and silanols of zeolite is critical for the development of high-performance zeolite catalysts.

Keywords: Zeolite; Silicalite-1; Silanol; Palladium; Dimethyl oxalate; Dimethyl carbonate

1. Introduction

Supported metal catalysts play a vital role in producing fuels and chemicals. The catalytic performance of the supported metal catalysts is dependent on three

interrelated factors, including the intrinsic properties of metal active sites, functionality of supports, and interactions between metals and supports [1–3]. These features make the supported metal catalysts sophisticated to be interpreted. Particularly, charge transfer between the metal and catalyst support, support-induced reconstruction of metal species, and the formation of specific metal-support interface could contribute to the metal-support interactions [4,5].

Zeolites with adjustable acid-base sites, unique structures, and well-defined pores and cages are extensively used as catalysts and supports [6,7]. In addition, silanols (Si–OH) are located in the internal and external surface of zeolites that can vary as types and amount depending on the properties of the zeolites. The formation of zeolite silanols originates from the crystallization process, different nature and purity of chemical reagents, and post-synthesis treatment [8,9]. The strategies employed to engineer silanol defects included the synthesis of layered zeolite, formation of mesopore, creation of defects by water intrusion, and the reduction of zeolite size [8,10,11]. In contrast, several methods are available to heal the silanol defects, such as heat treatment, radical-assisted approach, silane-modified method, blocking defects and incorporation of metal heteroatoms [12–14]. The zeolite silanol defects play an imperative role in setting the catalytic activity. Zhao et al. identified the decisive role of silanol defects in forming active ZnO_x species, and the ZnO-silicalite-1 showed three times higher yield than the commercial K-CrO_x/Al_2O_3 catalyst for the propane dehydrogenation [15]. Qi et al. reported that atomically dispersed Pt atoms could be

stably bonded with the nests of Zn atoms (≡SiOZn−OH) in dealuminated Beta zeolite, and the Pt-Zn-DeAlBeta catalyst exhibited excellent activity and stability for the propane dehydrogenation [16]. Li et al. found that Au atoms were homogeneously anchored through the condensation between −OH group of Au precursor and the silanols of pure silica zeolite [17]. Therefore, tuning the silanols of zeolites and understanding the interactions between silanols and metal species are of great interest in the field of catalysis.

To reduce the dependence on fossil resources, considerable research efforts were devoted to developing sustainable technologies for the catalytic conversion of one-carbon molecules (CO, CO_2, CH_4 and CH_3OH) into fuels and chemicals [18,19]. Dimethyl oxalate (DMO), $(CH_3OCO)_2$ is an industrial chemical intermediate with versatile properties. DMO is used as a solvent, extraction agent, and to produce ethylene glycol, ethanol, oxalic acid, oxamide, dyes and medicines [20,21]. Besides, dimethyl carbonate (DMC), $(CH_3O)_2CO$ is attracting lots of interest because of its excellent solubility, biodegradability and low toxicity. DMC could be used as green solvent, electrolytes in lithium batteries, potential fuel additive and for polycarbonate synthesis [22–24]. Therefore, the sustainable transformation of CO and CH_3OH to DMO and DMC is desirable for both fundamental research and commercial applications.

In the past decade, the indirect oxidative carbonylation of CH_3OH to DMO, i.e., CO coupling to DMO has been attracting considerable attention [25,26]. The world's

first plant of coal to DMO and further to ethylene glycol (0.2 million tons per year) was built in 2009; currently in China there are more than 28 plants with a total capacity of about 6 million tons [27]. For the Pd-based catalysts, the effects of support (α-Al_2O_3, MgO, ZnO, boehmite, layered double hydroxides and Nb_2O_5), shape and size of Pd nanoparticles, and promoters (Fe and Cu) have been intensively investigated on the DMO synthesis [28–30]. Recently, Tan et al. reported that hierarchical Nb_2O_5 with abundant oxygen defects was used to anchor the Pd species and thus enhanced the metal-support interactions [31]. Jing et al. found that the rich oxygen defects of layered double hydroxides promoted Pd clusters to bind with Zn- and Ti-based supports [32]. We have revealed that the Pd/α-Al_2O_3/Al-fiber catalyst not only showed high activity, but also decreased the hot-spot temperature of the catalyst bed due to enhanced thermal conductivity of structured Al-fiber [33].

The direct route of liquid-phase oxidative carbonylation of CH_3OH to DMC was commercialized by ENI company (Italy) in 1983 (details of Enichem process provided in Table S1 in Supporting Information (SI)) [34–36]. The liquid-phase reaction was carried out in a slurry reactor. The oxygen is the limiting reactant that should be lower than 4 vol% due to the explosive risk, where the CO is the excessive reactant. The Enichem process suffered from the difficult separation of the catalyst and the product, and azeotrope formation of CH_3OH/H_2O/DMC. To solve the problems of liquid-phase Enichem process, the indirect route of gas-phase oxidative carbonylation of CH_3OH to DMC was implemented by UBE company (Japan) in

1993 (details provided in Table S1) [36,37]. The indirect route is a two-step process, including DMC synthesis from CH_3ONO and CO, and non-catalytic regeneration of CH_3ONO from O_2, CH_3OH and recycled NO. The DMC synthesis was conducted in an anhydrous media to avoid the azeotrope formation. However, the chlorine-containing $PdCl_2$/active-carbon catalyst was used for DMC synthesis, and chlorine such as hydrogen chloride (100 μL L^{-1}) must be added to the reactants to slow down the deactivation of the catalyst (Table S1) [36,38]. The use of chlorine caused serious equipment corrosion, environmental pollution and difficulties related with product purification, obviously incompatible with the basic concepts of green chemistry. Thus, research efforts were devoted to the exploitation of the high-efficiency and chlorine-free catalysts on the DMC synthesis. Tan et al. demonstrated that the isolated Pd^{2+} centers were critical for the selective formation of DMC, while the aggregated Pd^0 centers resulted in the generation of DMO [39]. The Pd/NaY catalyst prepared by an ammonia-evaporation method showed high activity and stability of 100 h. Moreover, Wang et al. found that the tableting pressure could tune the Pd active sites in the Pd/NaY catalyst [40]. The Pd^0 species rather than Pd^{2+} improved the adsorption of CH_3ONO and CO reactants and thus increased the DMC selectivity. Yamamoto et al. reported that Pd/NaY catalyst showed a progressive deactivation, and the activity decreased by about 50% after 300 h catalytic test [41]. The main issue is the lack of sufficiently stable catalyst for the indirect oxidative carbonylation of CH_3OH to DMC [27,42].

As shown in Scheme 1, the Pd/α-Al_2O_3 catalyst has been successfully commercialized in the indirect oxidative carbonylation of CH_3OH to DMO. However, the chlorine-free Pd-based catalyst for single DMC synthesis could not be applied in the industry due to the unsatisfied stability. Herein, we present a novel process for indirect oxidative carbonylation of CH_3OH to co-synthesis of DMO and DMC. The process combined the advantages of the two separate routes of DMO and DMC syntheses (Scheme 2). The palladium containing silicalite-1 (Pd/S-1) catalyst was first used and showed to be highly active and stable for the co-synthesis of DMO and DMC. The results pointed out that the catalyst activation had a pronounced effect on the catalytic performance. Further, the synergistic interactions between the silanols of the S-1 zeolite and Pd species were studied by a series of in situ infrared experiments including the adsorption of CO, the change in the OH stretching vibrations, and the role of the silanols on CH_3ONO and CO adsorption.

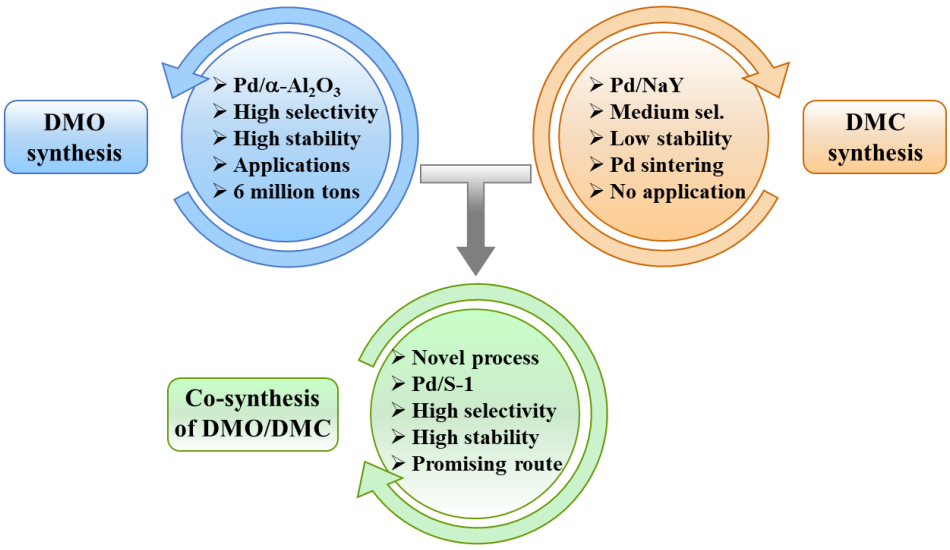

Scheme 1. The proposed novel co-synthesis of DMO and DMC based on two separate

routes of DMO and DMC syntheses.

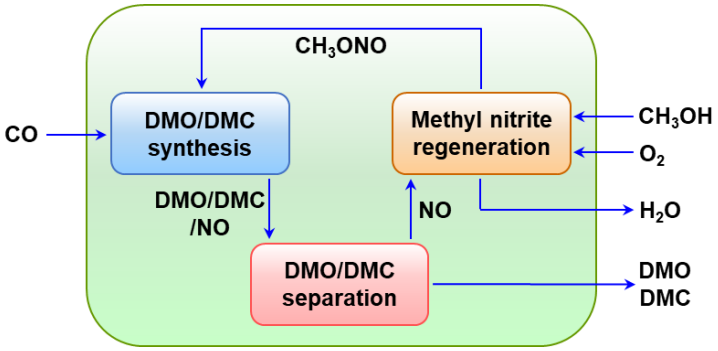

Scheme 2. Schematic presentation of potential process of the indirect oxidative carbonylation of methanol to co-synthesis of DMO and DMC.

2. Experimental

2.1. Catalyst preparation

The MFI-type and pure-silica silicalite-1 (S-1) zeolite was purchased from Nankai Catalyst Factory (China). The obtained S-1 zeolite was without the template. The catalyst was prepared by a vacuum-assisted method according to the following procedure. 0.0106 g palladium acetate ($Pd(CH_3COO)_2$, 47.0 wt% Pd, Sinopharm Chemical Reagent Co., Ltd., China) was dissolved in 1.2 g toluene ($C_6H_5CH_3$). S-1 zeolite was pre-dried at 110 °C for 12 h in a vacuum oven to remove the physically adsorbed water. 1.0 g S-1 zeolite was further pre-treated under vacuum for 2 h. Then, the resulting $Pd(CH_3COO)_2$ solution was added dropwise into the pre-treated S-1 zeolite. After stirring for 2 h, the sample was dried at 60 ºC for 8 h, and calcined for 2 h in the range of 200–500 ºC. As-obtained catalyst was denoted as Pd/S-1@*x*, where *x*

corresponds to the catalyst calcination temperature (for example, the catalyst calcined at 300 ºC was named as Pd/S-1@300). As reference supports, α-Al_2O_3, SiO_2 and zeolites (NaZSM-5, NaY, and NaBeta) were used for the preparation of catalysts following the same vacuum-assisted method. If not specified, the theoretical Pd loading and calcination temperature were 0.5 wt% and 300 ºC, respectively. The catalysts were tableted, crushed, and sieved into 60–80 mesh for the catalytic tests.

2.2. Catalyst characterizations

Transmission electron microscopy (TEM) images of the catalysts were acquired on a JEOL JEM-2100 TEM instrument. High-angle annular dark-field scanning transmission electron microscopy (HAADF-STEM) images were obtained on a spherical aberration-corrected Thermo Fisher Scientific Themis Z instrument; the elemental mapping was recorded on a Thermo Fisher Scientific Talos F200X S/TEM instrument equipped with an energy dispersive X-ray spectrometer (EDS). Scanning electron microscopy (SEM) images were obtained on a JEOL JSM-7900F SEM instrument. The actual Pd loading of catalyst was measured by inductively coupled plasma optical emission spectroscopy (ICP-OES) on an Agilent 720 ICP-OES. The solid-state ^{29}Si cross-polarization magic-angle spinning nuclear magnetic resonance (CP MAS NMR) and single pulse ^{29}Si MAS NMR spectra were measured on a Bruker Advance 400 spectrometer. X-ray diffraction (XRD) patterns were obtained using a Bruker D8 Advance diffractometer with Cu Kα radiation. Thermogravimetric-mass

spectrometry (TG-MS) was conducted using a gas mixture of 20 vol% O_2/N_2 on a Netzsch STA 449F5 instrument connected with QMS 403D mass spectrometer.

X-ray photoelectron spectroscopy (XPS) was conducted on an Escalab 250Xi spectrometer with an Al Kα radiation. The XPS spectra were calibrated according to the C 1s peak at 284.6 eV. The composition depth profile was recorded by sputtering with a focused 3 kV Ar^+ ion beam over an area of 4 mm^2.

Textural features of the samples were analyzed by N_2 adsorption/desorption isotherms at −196 ºC using a Quantachrome Autosorb-IQ3 instrument. The specific surface area was calculated via the Brunauer-Emmett-Teller (BET) equation; the pore size distribution was derived using the Barrett-Joyner-Halenda (BJH) model from the adsorption branch of the N_2 sorption isotherms; the micropore surface area and micropore volume were determined by the *t*-plot method.

H_2-temperature-programmed reduction (H_2-TPR) was carried out using a Tianjin Xianquan TP-5080-D apparatus. The H_2 consumption was monitored by a thermal conductivity detector (TCD). Typically, 0.100 g sample was pre-treated in He flow (30 mL min^{-1}) at 200 ºC for 1 h and then cooled down to 30 ºC. The H_2-TPR profiles were recorded in flowing 10 vol% H_2/N_2 at a heating rate of 10 ºC min^{-1}. A water trap was located before the TCD to avoid any H_2 signal perturbation.

CO pulse chemisorption was performed on an AutoChem Ⅱ 2920 instrument. 0.100 g sample was pre-treated in 99.99 vol% He flow (50 mL min^{-1}) at 200 ºC for 1 h and cooled down to 35 ºC. Afterward, 99.999 vol% CO gas was pulsed to the

reactor with an injection loop of 50 μL until the CO peak intensity remained unchanged.

The infrared experiments were conducted on a Bruker Vertex 70V spectrometer. A homemade cell fitted with BaF_2 windows was used for the diffuse reflectance infrared Fourier transform spectroscopy (DRIFTS) experiments with a mercury-cadmium-telluride (MCT) detector; another homemade cell equipped with KBr windows was employed for Fourier transform infrared (FTIR) experiments with a deuterated, L-alanine doped triglycine sulfate (DLaTGS) detector. The spectra were recorded in the range of 4000–600 cm^{-1} at a resolution of 4 cm^{-1} over 32 scans. A series of carefully-designed infrared experiments were carried out as follows. (1) DRIFTS spectra of CO adsorption (Figs. 8 and S15): typically, about 20 mg sample without diluents was pre-treated in N_2 flow (50 mL min^{-1}) at 200 ºC for 1 h and then cooled down to 35 ºC for taking a background spectrum. The adsorption of CO was conducted at 35 ºC using 99.999 vol% CO. After that, the sample was purged thoroughly with N_2 and then the DRIFTS spectra were collected at 35 ºC. (2) FTIR spectra in the OH-stretch region (Figs. 9 and S14): after the samples were degassed at the chosen temperatures for 2 h under vacuum (about 2 Pa), the FTIR spectra in the OH-stretch region were recorded with a self-supported zeolite pellet (diameter: 1.2 cm; weight: about 14 mg). (3) FTIR spectra of exposure to CO and CH_3ONO reactants (Figs. 11, S10, S11 and S12): a self-supported zeolite pellet was pre-treated in N_2 flow (50 mL min^{-1}) at 200 ºC for 1 h and then cooled down to 110 ºC for taking a spectrum.

The FTIR spectra were recorded after the exposure to 99.999 vol% CO for 5 minutes or CH_3ONO/N_2 (1/4, volume) for 10 minutes at 110 ºC. After a thorough N_2 purge, the FTIR spectra were recorded at 110 ºC. (4) FTIR spectra in the OH-stretch region against the catalyst calcination temperature (Fig. S13): a self-supported zeolite pellet was used; the FTIR spectra were continuously collected with increasing the calcination temperature of the IR reaction cell.

2.3. Catalytic tests

The schematic diagram of the experimental setup is shown in Scheme S1 (Supporting Information, SI). The reaction of indirect oxidative carbonylation of methanol to co-synthesis DMO and DMC using a fixed-bed, continuous-downflow quartz reactor (8 mm i.d.) operated at 0.1 MPa was performed. The 60–80 mesh catalyst was loaded into the middle of the quartz tube reactor between two layers of quartz wool. The methyl nitrite (CH_3ONO) reactant was synthesized in the laboratory by the esterification reaction ($2NaNO_2 + 2CH_3OH + H_2SO_4 \rightarrow 2CH_3ONO \uparrow + Na_2SO_4 + 2H_2O$). The feed gas of CH_3ONO was collected into a steel cylinder and then mixed with pure N_2 to obtain a gas mixture of CH_3ONO/N_2 (1/4, volume). Noted that the industrial synthesis of CH_3ONO is conducted with CH_3OH, O_2 and recycled NO, and the industrial use of CH_3ONO is self-closing and chemical-looping process (details provided in Scheme 2). The pure N_2, gas mixtures of CO/N_2 (1/9, volume) and CH_3ONO/N_2 (1/4, volume) were fed via three standard mass flow controllers. The

gas hourly space velocity (GHSV) was in the range of 8000–80000 mL $g_{cat.}^{-1}$ h^{-1}; $CO/CH_3ONO/N_2$ volume ratio was 1/6/33, i.e., 2.5, 15.0 and 82.5 vol%; reaction temperature ranged from 100 °C to 130 °C. No pre-treatment with H_2 was carried out in any of the catalytic tests. The product stream was analyzed by an online gas chromatography (Agilent 7890B). A thermal conductivity detector (TCD, 2.5-m 5A zeolite and 1.0-m HayeSep Q packed columns) was employed to identify CO and N_2; a flame ionization detector (FID, 30.0-m HP-Innowax capillary column) was used to analyze CH_3ONO, DMO, DMC, and methyl formate. The kinetic experiments and the calculations for turnover frequency (TOF), CH_3ONO conversion, CO conversion, DMO, DMC, and methyl formate selectivity were presented in SI.

3. Results and discussion

3.1. Catalytic performance of Pd/S-1 catalyst for co-synthesis of dimethyl oxalate and dimethyl carbonate

A vacuum-assisted method was used to anchor the Pd species on the zeolite support as described above. The key feature was to activate the zeolite prior to contacting with the Pd precursor. The Pd solution was easily adsorbed on the zeolite due to the capillary action [43]. The catalytic activities of different Pd-based catalysts prepared by the vacuum-assisted method are summarized in Table 1. Since the acidic supports are unsuitable for DMO and DMC syntheses [30], α-Al_2O_3 and SiO_2 were selected as representative neutral oxide supports, and pure-silica S-1, NaZSM-5, NaY

and NaBeta zeolites were also chosen. As shown in Table 1, the Pd/S-1@300 catalyst delivered the highest CO conversion and DMO+DMC selectivity among all the Pd catalysts. The low DMO+DMC selectivity of Pd/α-Al_2O_3, Pd/NaZSM-5, Pd/NaY and Pd/NaBeta resulted from the decomposition of CH_3ONO reactant ($4CH_3ONO \rightarrow CHOOCH_3 + 2CH_3OH + 4NO$) [44]. The results demonstrated that the catalytic activity of co-synthesis of DMO and DMC was strongly dependent on the properties of catalyst support.

Table 1 Catalytic performance of different Pd-based catalysts for co-synthesis of DMO and DMC.[a]

Catalyst[b]	Conversion (%)		Selectivity (%)		
	CO	CH_3ONO	DMO	DMC	DMO+DMC
Pd/S-1	77.1	17.9	75.0	21.9	96.9
Pd/α-Al_2O_3	15.2	11.5	6.9	37.9	44.8
Pd/SiO_2	35.1	8.3	75.0	14.9	89.9
Pd/NaZSM-5(24.7)[c]	5.6	8.1	4.2	18.8	23.0
Pd/NaZSM-5(298.6)[c]	16.3	11.6	5.0	43.7	48.7
Pd/NaY(2.7)[c]	66.8	39.0	0.0	62.8	62.8
Pd/NaBeta(12.5)[c]	18.8	43.8	0.0	15.7	15.7

[a] Reaction conditions: $CO/CH_3ONO/N_2$ = 1/6/33 (volume), 110 ºC, GHSV of 8000 mL $g_{cat.}^{-1}$ h^{-1}, 0.100 g catalyst.

[b] Catalysts prepared by the vacuum-assisted method with 0.5 wt% Pd.

[c] Pd/NaZSM-5(24.7), Pd/NaZSM-5(298.6), Pd/NaY(2.7) and Pd/NaBeta(12.5) catalysts with Si/Al molar ratio of 24.7, 298.6, 2.7 and 12.5, respectively.

The effects of reaction temperature, palladium loading, and catalyst calcination temperature were studied for the co-synthesis of DMO and DMC (Fig. 1). As shown in Fig. 1a, with increasing reaction temperature from 110 °C to 130 °C, both CO and CH_3ONO conversion gradually increased while DMO+DMC selectivity decreased from 99.0% to 83.0%. The CO conversion was remarkably enhanced from 26.9% to 74.1% by increasing palladium loading from 0.2 wt% to 0.35 wt%, and increased to 91.7% at the palladium content of 1.5 wt% (Fig. 1b). If both the catalytic performance and catalyst cost are considered, the optimal palladium loading for the catalyst is 0.5 wt%. The actual palladium content was measured to be 0.47–0.48 wt% by ICP-OES analysis (Table 2). As shown in Fig. 1c, the Pd/S-1 catalysts calcined at 200 °C and 300 °C showed much higher CO, CH_3ONO conversion and DMO+DMC selectivity than the ones at 400 °C and 500 °C. With increasing calcination temperature from 300 °C to 400 °C, the CO conversion drastically decreased from 77.1% to 11.4%, and DMO+DMC selectivity decayed from 96.9% to 63.9%. Similar effect for the catalysts with a palladium loading of 1.0 wt% was also observed (Fig. 1d). The results suggested that the calcination temperature of Pd/S-1 catalyst had a very pronounced effect on the catalytic performance (Fig. 1c,d).

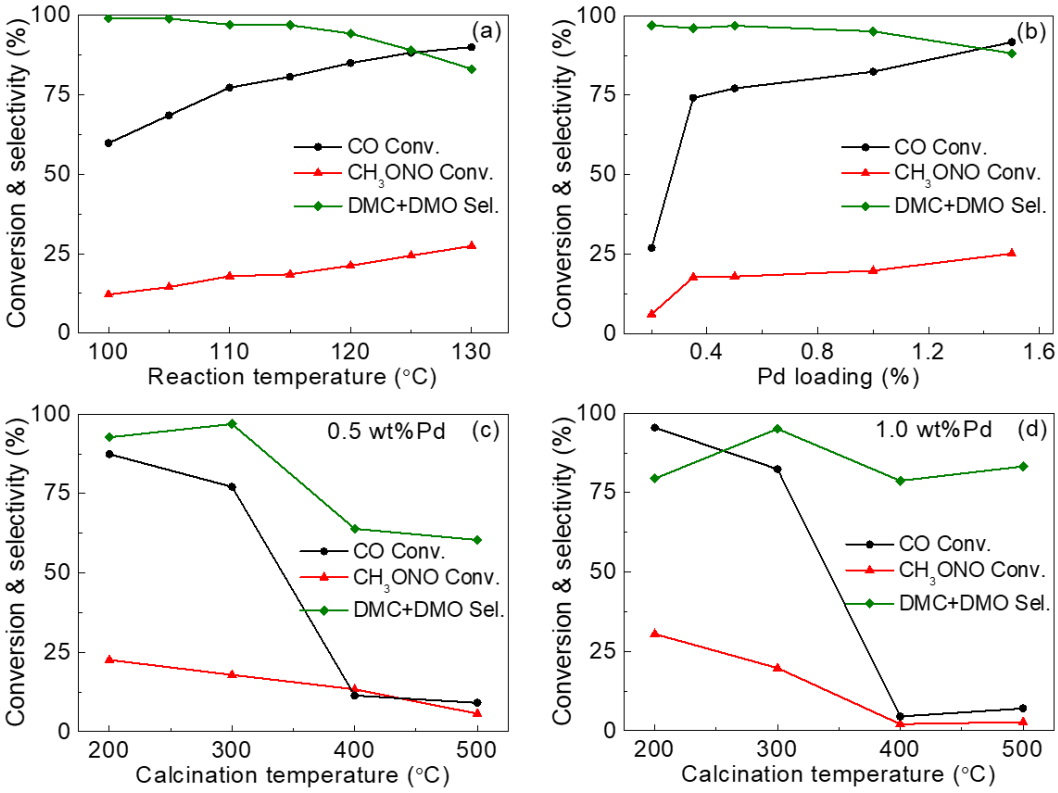

Fig. 1. Effects of reaction temperature and preparation parameters on the catalytic activity of Pd/S-1 catalyst for the co-synthesis of DMO and DMC: (a) reaction temperature; (b) palladium loading; (c) calcination temperature of the catalyst with 0.5 wt% Pd; (d) calcination temperature of the catalyst with 1.0 wt% Pd. Reaction conditions: $CO/CH_3ONO/N_2$ = 1/6/33 (volume), GHSV of 8000 mL $g_{cat.}^{-1}$ h^{-1}, 0.100 g catalyst. The theoretical Pd loading, reaction temperature and calcination temperature of the catalyst are 0.5 wt%, 110 °C and 300 °C, if not specified.

The kinetic experiments were carried out to obtain the apparent activation energy and TOF after eliminating both internal and external diffusion. The Pd/S-1 catalysts calcined at 200, 300, 400 and 500 °C with an actual Pd content of about 0.47 wt% denoted as Pd/S-1@200, Pd/S-1@300, Pd/S-1@400 and Pd/S-1@500, respectively

were studied. The Pd/S-1@200 and Pd/S-1@300 showed the low apparent activation energy of 51 and 52 kJ mol^{-1}, while the Pd/S-1@400 and Pd/S-1@500 were 89 and 101 kJ mol^{-1} (Fig. 2). The big difference among the apparent activation energies suggested that the reaction pathway and rate-controlling step were possibly different for catalysts Pd/S-1@200, Pd/S-1@300 *vs.* Pd/S-1@400, Pd/S-1@500 [45,46]. The TOF of Pd/S-1@200 and Pd/S-1@300 was two times larger than Pd/S-1@400 and Pd/S-1@500 (0.18 *vs.* 0.06 s^{-1}; Table 2). The apparent activation energy and the TOF confirmed that catalyst calcination temperature played a critical role in the activity.

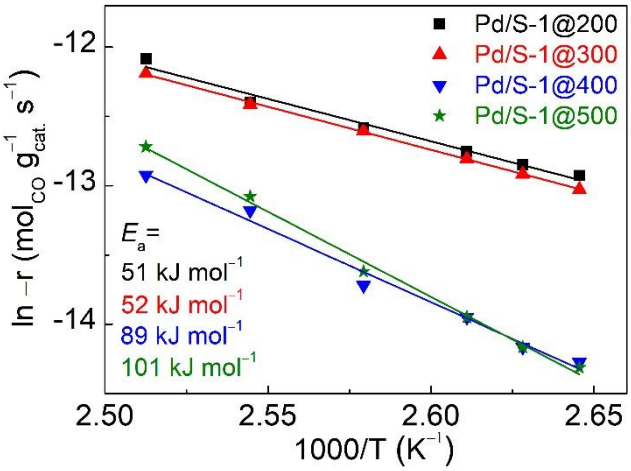

Fig. 2. Arrhenius plot for the co-synthesis of DMO and DMC using Pd/S-1 catalyst activated at different temperatures (E_a, apparent activation energy). Reaction conditions: $CO/CH_3ONO/N_2$ = 1/6/33 (volume), GHSV of 80000 mL $g_{cat.}^{-1}$ h^{-1}, 0.010 g catalyst with 0.090 g α-Al_2O_3 (diluent).

Table 2 Physicochemical properties of Pd/S-1 catalyst obtained at different calcination temperatures, and their catalytic performance.

Sample	S_{BET} ($m^2\ g^{-1}$)[a]	S_{micro} ($m^2\ g^{-1}$)[a]	V_{micro} ($cm^3\ g^{-1}$)[a]	Pd (wt%)[b]	Pd size (nm)[c]	CO adsor. ($mmol_{CO}\ g_{cat.}^{-1}$)[d]	E_a (kJ mol^{-1})	TOF (s^{-1})
S-1 support	491.0	453.0	0.23	—	—	—	—	—
Pd/S-1@200	393.3	354.3	0.15	0.47	3.0	0.013	51	0.18
Pd/S-1@300	405.4	361.6	0.16	0.48	3.2	0.010	52	0.18
Pd/S-1@400	456.3	413.1	0.18	0.47	3.3	0.005	89	0.06
Pd/S-1@500	390.2	367.5	0.18	0.48	3.5	0.002	101	0.06

[a] BET surface area measured by BET equation, the micropore surface area and volume calculated through the *t*-plot method.

[b] Palladium content measured by ICP-OES.

[c] Average size obtained by TEM images.

[d] Number of adsorbed CO determined by CO pulse experiments at 35 ºC.

Based on the above results, the optimal reaction temperature, palladium loading and calcination temperature identified were 110 °C, 0.5 wt% and 300 °C, respectively. The catalyst calcination temperature significantly affected the catalytic activity of the Pd/S-1 that needed to be further studied.

3.2. Properties of Pd/S-1 catalyst calcined at different temperatures

Various characterization techniques were employed to study the calcination-temperature-dependent activity. The morphology of the Pd/S-1 catalyst calcined at 200, 300, 400 and 500 ºC was examined by SEM (Figs. 3 and S1). Each

catalyst consisted of coffin-shaped and uniform crystals. The N_2 adsorption-desorption isotherms displayed a mixture of type- Ⅰ and -Ⅳ isotherms (Fig. S2). The unique hysteresis loop at a low P/P_0 of 0.05–0.2 is due to the presence of silanol defects [47,48]. These four Pd/S-1 catalysts showed a BJH mesopore size of 2–5 nm, confirmed by the hysteresis loop at P/P_0 of 0.4–0.6 (Fig. S2). After loading the Pd by vacuum-assisted method, the S_{micro} surface area of the Pd/S-1@200 catalyst decreased from 453.0 m^2 g^{-1} to 354.3 m^2 g^{-1} (Table 2). This suggested that the Pd precursor possibly entered in the pores of the zeolite (S-1). With increasing calcination temperature from 200 °C to 400 °C, the S_{BET}, S_{micro} and V_{micro} gradually increased, while Pd/S-1@500 catalyst showed the lower S_{BET} and S_{micro} (Table 2). These results demonstrated that the crystal morphology and textural properties were not associated with the catalytic activity.

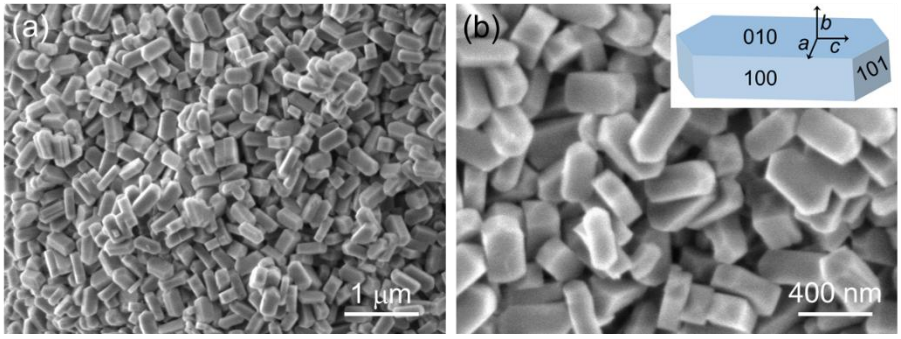

Fig. 3. SEM images of (a, b) the Pd/S-1@300 catalyst. *Inset*: crystal dimensions.

As shown in Fig. 4, all four catalysts exhibited the characteristic diffraction peaks of MFI topology (JCPDS 44-0696). Compared to the catalysts before the catalytic test, the dual diffraction peaks overlapped into a single peak on the catalysts after the

catalytic test (23.3°, 23.4°→ 23.3°, 23.7°, 23.9°→ 23.7°, 24.4°, 24.6°→ 24.4°; Fig. 4 B,C). The peak overlap was indicative of the change from a monoclinic phase to an orthorhombic phase [12,13]. When the molecules (kinetic diameter ≈ maximum pore size) were adsorbed in the S-1 zeolite, the adsorption would lead to a symmetry change of S-1 zeolite from monoclinic with space group $P2_1/n11$ to orthorhombic with $P2_12_12_1$ [49,50]. Consequently, the phase transition of monoclinic-to-orthorhombic was ascribed to the adsorbed reaction species during the catalytic test (Fig. 4 B,C). Moreover, the thermal behavior of the catalysts was evaluated using TG-MS (Fig. S3). No further signals above 400 °C were detected thus suggesting that no carbon was deposited on all four catalysts [51,52]. The TG-MS results indicated that the low activity of Pd/S-1@400 and Pd/S-1@500 catalysts could not be ascribed to the carbon deposits and residual reaction species.

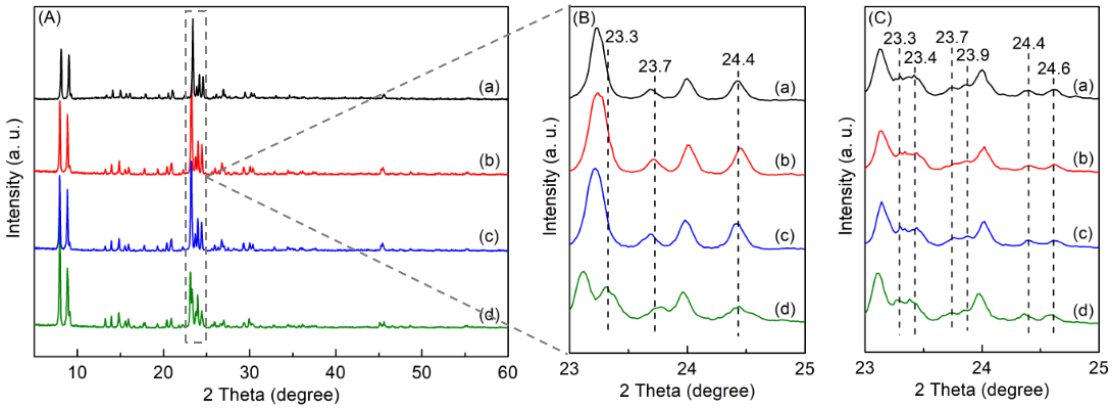

Fig. 4. XRD patterns of the catalysts (A, B) after 3 h catalytic test and (C) prior to the catalytic test: (a) Pd/S-1@200, (b) Pd/S-1@300, (c) Pd/S-1@400 and (d) Pd/S-1@500.

The TEM images showed the aligned lattice fringes revealing the good crystallinity of the S-1 zeolite (Fig. 5). The Pd/S-1@200, Pd/S-1@300, Pd/S-1@400 and Pd/S-1@500 catalysts exhibited a similar Pd distribution with an average size of 3.0, 3.2, 3.3 and 3.5 nm, respectively. Indeed, the high dispersion of Pd was also confirmed by XRD (Fig. S5). No Bragg peaks expected for Pd^0 (JCPDS 01-1201) and PdO (JCPDS 88-2434) were detected (Fig. S5). In addition, the HAADF-STEM and elemental mapping of Si, O and Pd further verified the high dispersion of Pd (Fig. 6). The TEM, HAADF-STEM and XRD results suggested that the calcination temperature had a negligible effect on the Pd size and distribution.

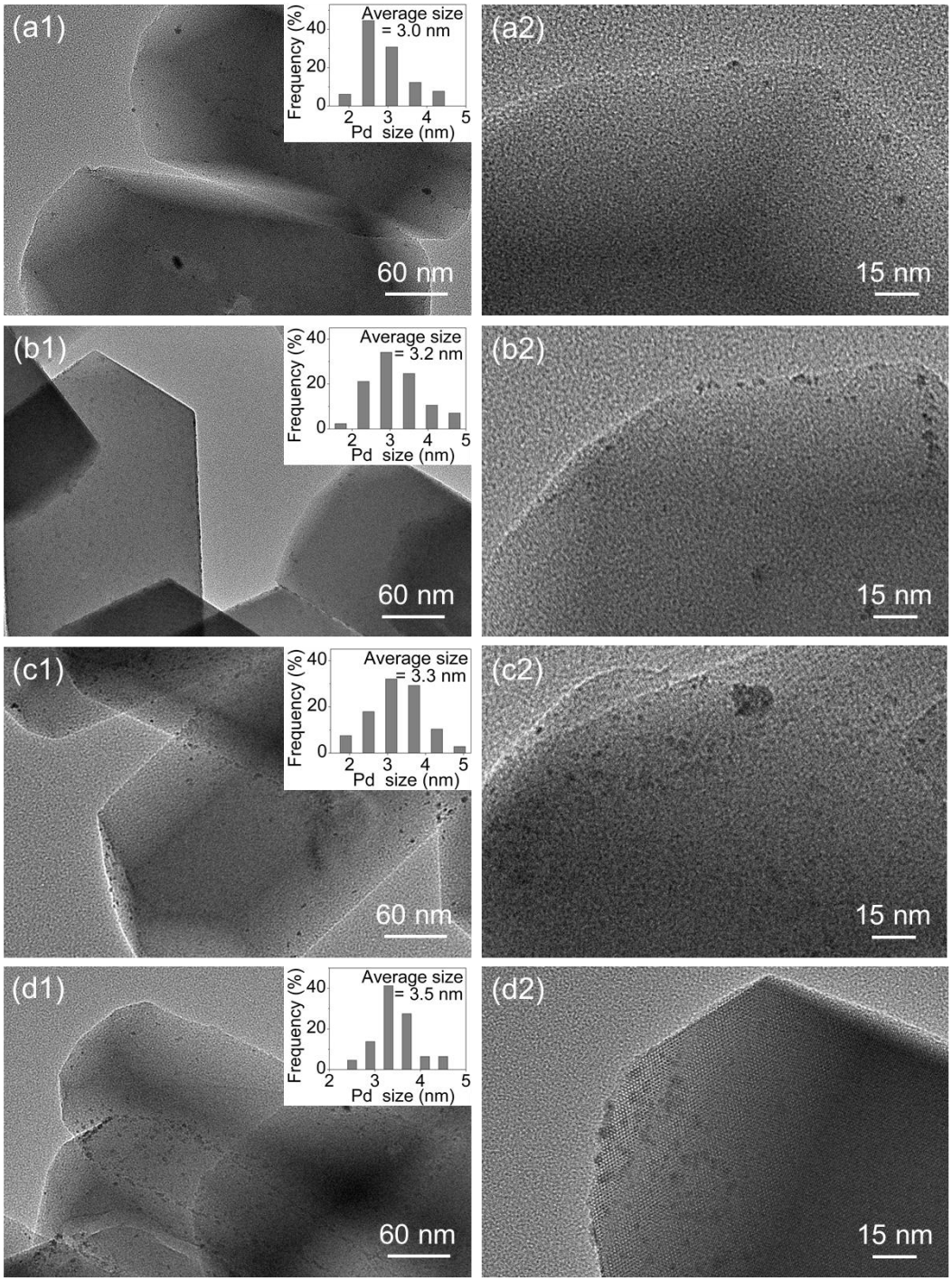

Fig. 5. TEM images of the used catalysts: (a1, a2) Pd/S-1@200, (b1, b2) Pd/S-1@300, (c1, c2) Pd/S-1@400 and (d1, d2) Pd/S-1@500. *Inset* of (a1), (b1), (c1) and (d1): size distribution of Pd nanoparticles.

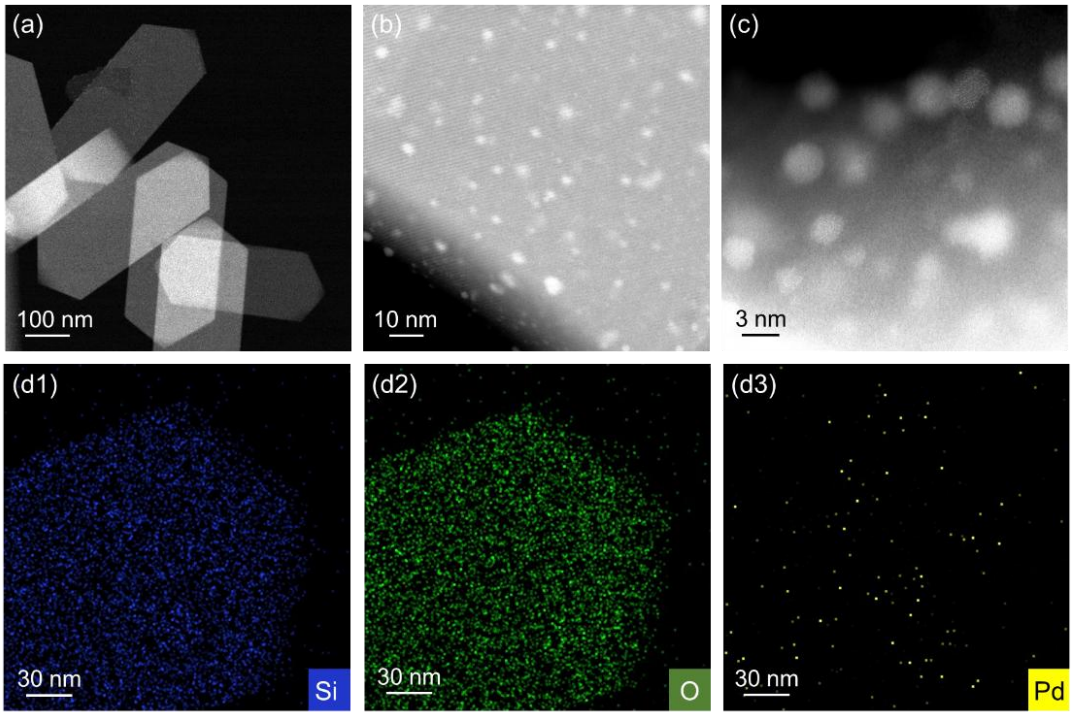

Fig. 6. (a–c) aberration-corrected HAADF-STEM images and (d1–d3) HAADF-STEM-EDS elemental mapping of Si (blue), O (green) and Pd (yellow) on the used Pd/S-1@300 catalyst.

The effect of catalyst calcination temperature on the valence state of Pd species was evaluated by XPS. The Pd, Si, O and C elements were detected on the XPS survey spectra (Fig. 7A). The high-resolution Pd 3d spectra contained the $3d_{5/2}$ and $3d_{3/2}$ peaks with spin-orbit splitting of about 5.3 eV (Fig. 7B). Since the binding energies of 336.7 and 338.0 eV were 0.7–1.2 eV larger than the ones expected for Pd^0 and Pd^{2+} species, they were attributed to $Pd^{\delta+}$ and $Pd^{(2+\delta)+}$ species ($0 < \delta \leq 2$) [40]. Similar assignments of $Pd^{\delta+}$ and $Pd^{(2+\delta)+}$ species were reported previously [53,54]. The increase of binding energies was due to the Lewis acid sites of S-1 zeolite, which were electron acceptors and thus caused the Pd species to lose the electrons [52,55].

The $Pd^{(2+\delta)+}/(Pd^{\delta+}+Pd^{(2+\delta)+})$ ratio for Pd/S-1@200, Pd/S-1@300, Pd/S-1@400 and Pd/S-1@500 catalysts were 50%, 53%, 40% and 44%, respectively based on the XPS spectra (Table S2). This result was consistent with the H_2-TPR experiments revealing the high-temperature reduction peak areas for Pd/S-1@200, Pd/S-1@300 catalysts in comparison to Pd/S-1@400, Pd/S-1@500 catalysts (Fig. S6). Thus, the XPS and H_2-TPR results suggested that similar valence state of Pd species was not responsible for the calcination-temperature-dependent activity. In addition, these four catalysts exhibited the surface Pd content of 0.69–1.08 wt% as measured by the XPS surface technique (Table S2), which was higher than the overall Pd content of 0.47–0.48 wt% measured by ICP-OES (Table 2). Sputtering with an Ar^+ beam was performed to gain insight into the Pd distribution in the Pd/S-1@300 catalyst. With increasing the sputtering time from 0 s to 60 s, the peak area of Pd species decreased gradually and remained almost stable with further increasing the time to 180 s (Fig. S7). Assuming the theoretical sputtering rate was 1 nm s^{-1}, the Pd species were mainly located on the surface of 60 nm in the catalyst [56]. This result is in accordance with decreased surface area (S_{micro}) measured by N_2 adsorption (Table 2). Both results, the XPS with Ar^+ sputtering and the N_2 adsorption indicated that the Pd species penetrated to the pores of S-1 zeolite using the vacuum-assisted method.

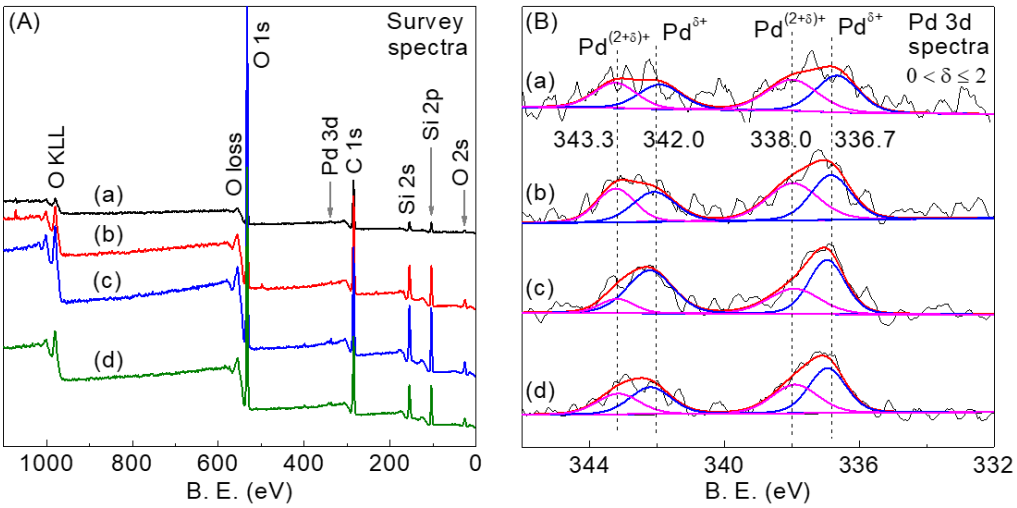

Fig. 7. (A) XPS survey spectra and (B) high-resolution palladium 3d spectra of the used catalysts: (a) Pd/S-1@200, (b) Pd/S-1@300, (c) Pd/S-1@400 and (d) Pd/S-1@500.

3.3. Synergistic interactions of silanols and Pd

Carbon monoxide is not only one of the reactants for the co-synthesis of DMO and DMC but also a widely used probe molecule. Fig. 8 shows the background-subtracted DRIFTS spectra of Pd/S-1 catalyst exposed to CO. The band at 2128/2130 cm^{-1} could be attributed to the linear CO adsorbed on the $Pd^{(2+\delta)+}$ species; the bands at 2086 cm^{-1} and 1939/1945 cm^{-1} were assigned to the linear CO and bridged CO adsorbed on the $Pd^{\delta+}$ species (Fig. 8) [40,57]. The intensities of CO adsorption bands on both fresh and used Pd/S-1@200 and Pd/S-1@300 catalysts were stronger than the Pd/S-1@400 and Pd/S-1@500. Besides, according to the CO pulse chemisorption (Fig. S8), the number of adsorbed CO was determined to be 0.013, 0.010, 0.005 and 0.002 $mmol_{CO}\ g_{cat.}^{-1}$ on the Pd/S-1@200, Pd/S-1@300, Pd/S-1@400

and Pd/S-1@500 catalysts, respectively (Table 2). In comparison with fresh Pd/S-1@200 and Pd/S-1@300 catalysts, the linear CO bands at 2130 cm^{-1} and 2086 cm^{-1} were clearly increased on the used catalysts (Fig. 8). This was possibly related to the high catalytic activity. The DRIFTS spectra of CO adsorption and CO pulse chemisorption indicated that the adsorbed CO on the Pd/S-1@200 and Pd/S-1@300 catalysts was much larger than the Pd/S-1@400 and Pd/S-1@500 catalysts (Fig. 8 and Table 2). This was in line with the catalytic performance: high TOF of Pd/S-1@200, Pd/S-1@300 *vs.* low TOF of Pd/S-1@400, Pd/S-1@500 (Table 2). The adsorption of CO reactant is essential for the formation of DMO and DMC following the Langmuir-Hinshelwood mechanism [58,59]. Thus, the enhanced adsorption of CO reactant can be considered as a critical descriptor of the high activity.

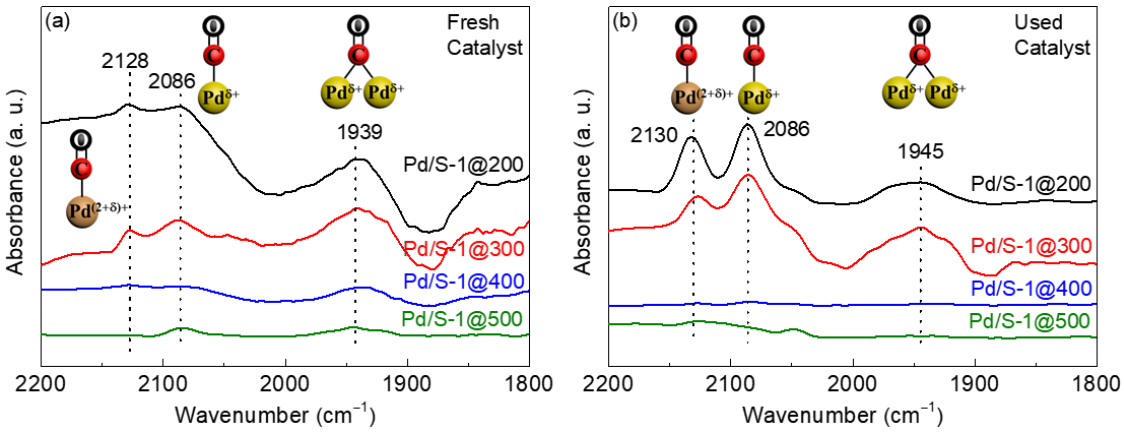

Fig. 8. DRIFTS spectra of CO adsorbed on (a) fresh and (b) used catalysts at 35 ºC.

Because of the similar Pd nanoparticle size, Pd valence state and equivalent Pd content, the high intrinsic activity with enhanced CO adsorption was initially

attributed to the different properties of the catalyst support. As previously stated, the catalyst morphology, crystallinity, textural properties and residual reaction species were not associated with the catalytic activity. As well known, the heat treatment is a common method applied to heal silanols in zeolites through the condensation reaction [8]. It was thus reasonable to infer that the silanols of zeolite might be essential to the calcination-temperature-dependent activity through the silanol-Pd synergistic interactions. The FTIR spectra in the OH-stretch region are shown in Fig. 9. The bands at 3736 cm^{-1} and 3720 cm^{-1} were assigned to the external and internal isolated silanols; the bands at 3682 cm^{-1} and 3475 cm^{-1} corresponded to vicinal silanols and silanol nests, respectively [17]. With increasing the calcination temperature for the catalyst, the external and internal isolated silanols remained stable; the silanol nests gradually decreased while the vicinal silanols increased (Fig. 9). By increasing the temperature of thermal treatment, a progressive condensation of silanol nests occurred accompanied by the formation of new Si–O–Si bridges and water [60]; the silanol nests were partially converted to the vicinal silanols, as schematically shown in Scheme S2. Most obviously, the number of silanol nests on the Pd/S-1@200 and Pd/S-1@300 catalysts were higher than the Pd/S-1@400 and Pd/S-1@500 (Fig. 9). Besides, the evolution of silanols was studied by ^{29}Si NMR spectroscopy (Fig. 10). The resonance peak at −113 ppm was assigned to Q^4 [$(OSi)_4$], while the peaks at −106 ppm and −102 ppm corresponded to Q^3 [$HO–Si(OSi)_3$] [61,62]. The intensity of the resonance peaks at −106 ppm and −102 ppm was considerably enhanced on the ^{29}Si

CP MAS NMR spectra (Fig. S9). This indicated the presence of H–Si dipolar interactions due to the silanols of Q^3 species [63]. The resonance peak of Q^3 species at –106 ppm on the Pd/S-1@300 catalyst was higher than the counterpart on the Pd/S-1@400 (Fig. 10). This confirmed that the silanols were partially healed at the high calcination temperature, which was in accordance with the FTIR results (Fig. 9).

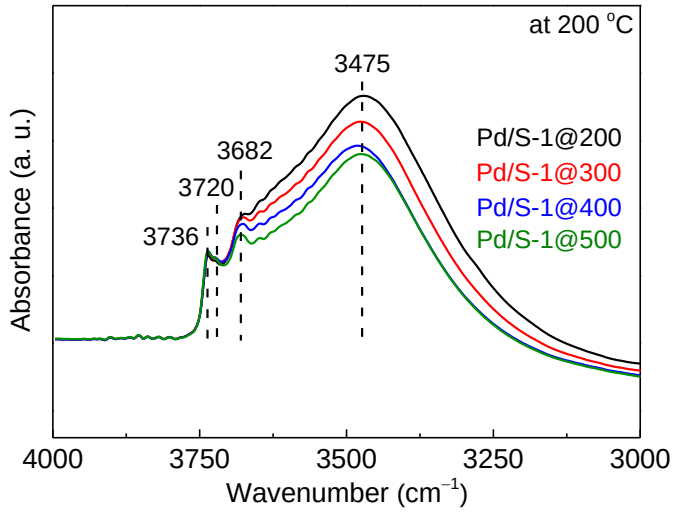

Fig. 9. FTIR spectra in the OH-stretch region of the used catalysts outgassed under vacuum at the appointed temperature and measured at 200 ºC. The outgas temperature for Pd/S-1@200, Pd/S-1@300, Pd/S-1@400 and Pd/S-1@500 catalysts was 200, 300, 400 and 500 ºC, respectively and consistent with the catalyst calcination temperatures.

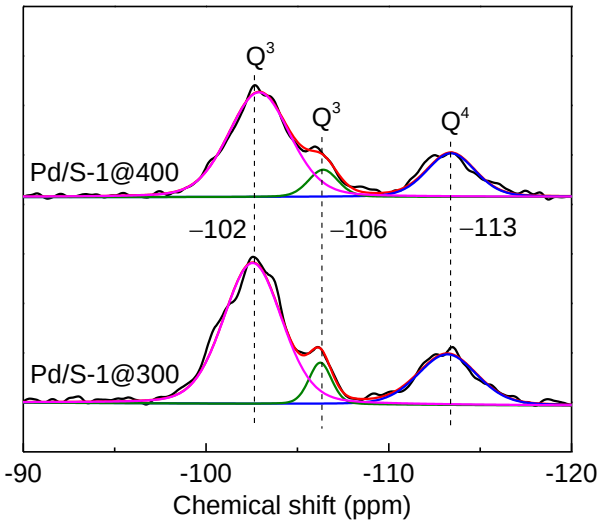

Fig. 10. Solid-state ^{29}Si CP MAS NMR spectra of the used Pd/S-1@300 and Pd/S-1@400 catalysts.

As discussed above, CO adsorption was enhanced on the Pd/S-1 catalyst with abundant silanols content. The role the silanols in CO adsorption is of great interest. Fig. 11 shows the FTIR spectra of Pd/S-1@300, Pd/S-1@400 catalysts and S-1 zeolite before and after exposure to CO. In the case of switching from N_2 to CO at 110 ºC for the Pd/S-1@300 catalyst, the typical dual bands at 2172 cm^{-1} and 2117 cm^{-1} corresponding to gaseous CO were observed. The band corresponding to the silanol nests was shifted by –10 cm^{-1} (Fig. 11a), while only small shifts of –3 cm^{-1} and –2 cm^{-1} for the Pd/S-1@400 and S-1 zeolite were detected (Fig. 11b,c). As well known, the interactions between CO and silanols are essentially electrostatic. The CO-induced shift of ν(OH) is typically about –300 cm^{-1} resulting from the formation of OH–CO complexes (C-bonded CO with OH). A shift of ν(OH) to –40 cm^{-1} corresponds to the formation of isocarbonyls of OH–OC complexes (O-bonded CO with OH). The

formation of OH–CO or OH–OC complexes usually occurred at extremely low temperature, e.g., −173 ºC [64–66]. Consequently, the shift of −10 cm^{-1} for the Pd/S-1@300 could not be assigned to the formation of OH–CO or OH–OC complexes. Moreover, the shift for Pd/S-1@300 was higher than that for Pd/S-1@400 and S-1 zeolite (Fig. 11). As previously stated, the number of adsorbed CO on the Pd/S-1@300 catalyst was much larger than on the Pd/S-1@400 (Fig. 8 and Table 2). It was thus reasonable to infer that the CO adsorption over the catalyst possibly changed the silanol-Pd synergistic interactions and thus caused the shift of silanols. In addition, all the CO-adsorption-induced shifts of ν(OH) on samples Pd/S-1@300, Pd/S-1@400 and S-1 disappeared after the N_2 purge (Fig. S10). This further confirmed that the shift of ν(OH) was associated with CO adsorption. Most obviously, the significant baseline shift of Pd/S-1@300 appeared after exposure to CO, while only a tiny baseline shift was observed on the Pd/S-1@400 and S-1 samples (Fig. 11). The significant baseline shift is attributed to the abundant adsorption of CO and change of properties of Pd/S-1@300 catalyst [67,68]. The FTIR spectra of Pd/S-1@300 and Pd/S-1@400 catalysts before and after exposure to CH_3ONO were presented in Figs. S11 and S12. The band corresponding to the silanol nests shifted by +9 cm^{-1} on both Pd/S-1@300 and Pd/S-1@400 catalysts (Fig. S11). The shift was possibly attributed to the silanol-catalyzed decomposition of CH_3ONO reactant and/or the impurity of gaseous water formed during the synthesis of CH_3ONO [20]. The results suggested that the adsorption of CH_3ONO reactant was not associated with the

different activity of the Pd/S-1@300 and Pd/S-1@400 catalysts.

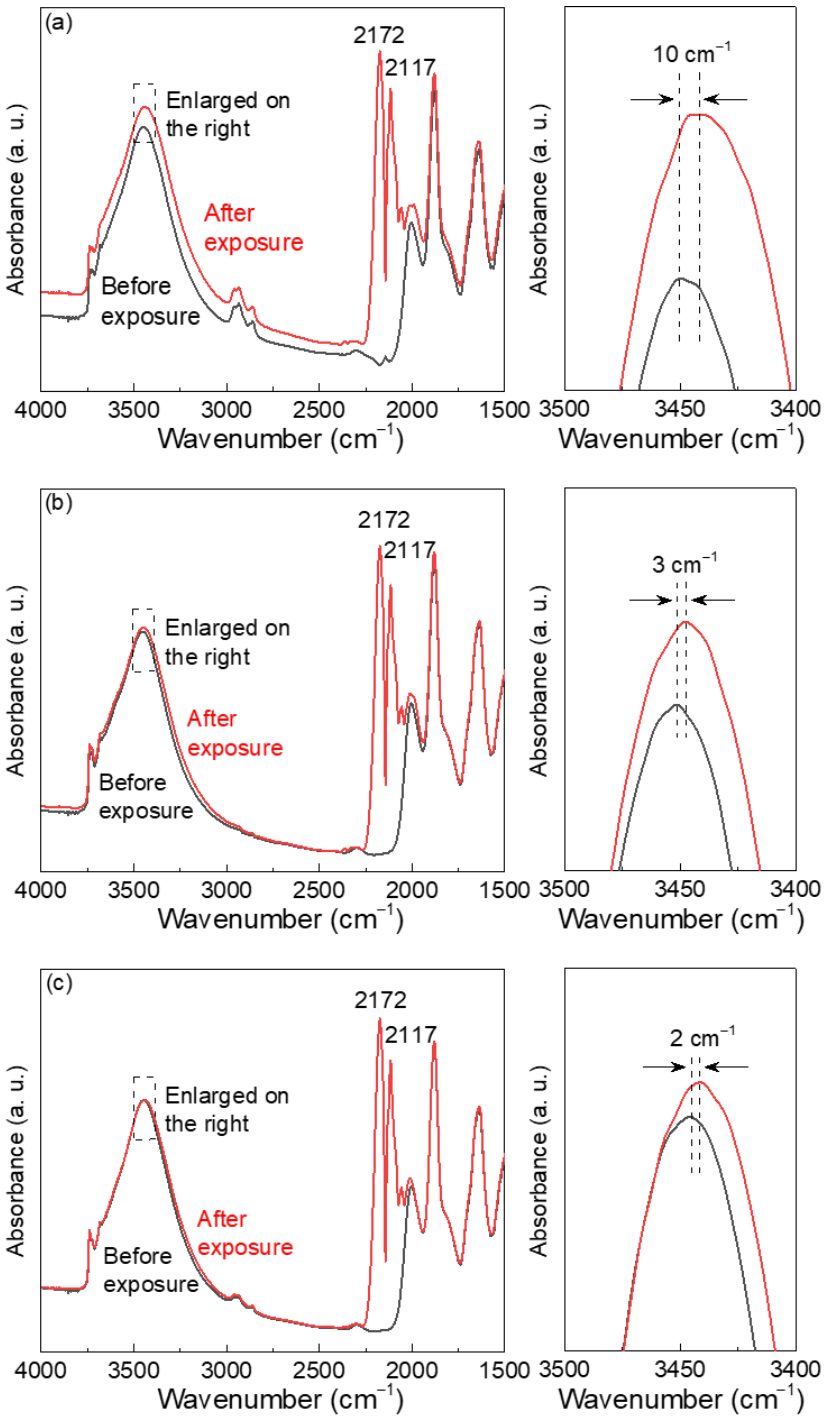

Fig. 11. FTIR spectra of (a) Pd/S-1@300, (b) Pd/S-1@400 and (c) S-1 zeolite before and after the exposure to CO at 110 ºC.

In order to investigate the silanol-Pd synergistic interactions, the catalyst calcination was monitored by in situ FTIR. By increasing the calcination temperature, a progressive decrease of silanols were observed on all samples, the S-1 zeolite, Pd/S-1 with a Pd loading of 0.5 wt% and 3.0 wt% (Fig. S13). The sole S-1 zeolite showed a decreased slope of 0.214 on the plot of FTIR band area of silanols *vs.* calcination temperature, while the Pd/S-1 catalysts with 0.5 wt% and 3.0 wt% Pd exhibited the larger decrease slope of 0.228 and 0.252, respectively (Fig. S13). The observation should be closely related to the Pd species. This suggested that the Pd species possibly reacted with surrounding silanols to form the PdO_x during the catalyst calcination. Similar phenomena were also observed for Zn and Au with silanols on the S-1 zeolite [15,17]. As previously stated, the silanols were essential for the catalyst activity through the silanol-Pd synergistic interactions. The tungsten-containing S-1 (W-S-1) was synthesized according to the procedure described elsewhere [12]. The introduction of tungsten prevented the formation of silanol nests as evidenced by FTIR in the OH-stretch region (Fig. S14). As predicted, the Pd/W-S-1 with 0.5 wt% Pd showed a very low CO and CH_3ONO conversion of 2.4% and 4.3%. This could be ascribed to the much lower CO adsorption on the Pd/W-S-1 catalyst than the Pd/S-1@300 (DRIFTS spectra of CO adsorption in Fig. S15). Based on the above results, we suggest that the Pd-silanol interactions are vital for the enhanced catalytic performance for the co-synthesis of DMO and DMC.

3.4. Stability of Pd/S-1 catalyst

The long-term stability test of the best performing Pd/S-1@300 catalyst is depicted in Fig. 12. As shown, the catalytic activity of the Pd/S-1@300 catalyst did not change during 200 h catalytic test. The catalyst exhibited CO conversion of 78.1 ± 0.5%, CH_3ONO conversion of 18.8 ± 0.8%, and DMO+DMC selectivity of 96.4 ± 0.5% with a molar DMO/DMC ratio of 3.1. The conversion and product selectivity remained stable, confirming the excellent stability of Pd/S-1@300 catalyst. The used catalyst was examined by XRD (Fig. S16). No Bragg peaks of Pd^0 (JCPDS 01-1201) and PdO (JCPDS 88-2434) were detected on the Pd/S-1@300 catalyst after 200 h test. The average size of Pd nanoparticle was 3.1 nm, which was very close to the catalyst after 3 h (3.2 nm) (Figs. 5b and S17). Both XRD and TEM results indicated the high Pd dispersion and excellent resistance to sintering. Moreover, in comparison with the commercial oxidative carbonylation of CH_3OH to DMC reported by ENI and UBE companies, the indirect route of co-synthesis of DMO and DMC shows several advantages such as chlorine-free catalyst, excellent stability and no risk of explosion (Table S1).

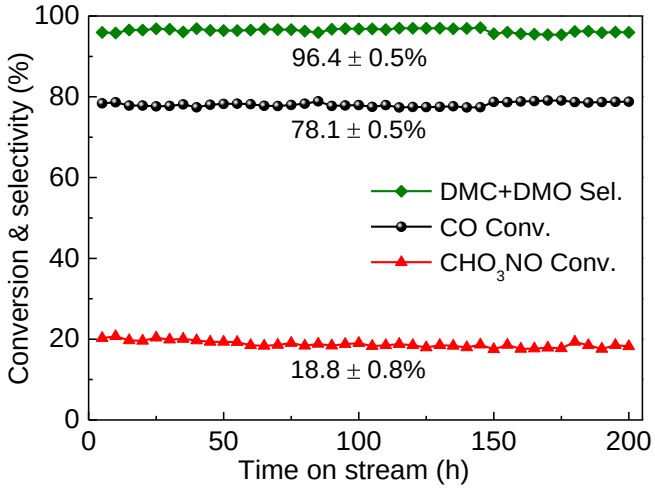

Fig. 12. Stability test on the Pd/S-1@300 catalyst for the co-synthesis of DMO and DMC. Reaction conditions: 110 °C, $CO/CH_3ONO/N_2$ = 1/6/33 (volume), GHSV of 8000 mL $g_{cat.}^{-1}$ h^{-1}, 0.100 g catalyst.

4. Conclusions

The indirect oxidative carbonylation of CH_3OH to co-synthesis DMO and DMC using Pd/S-1 catalyst is a new promising route due to its high activity and excellent stability. The Pd/S-1 catalyst with abundant silanols exhibited a higher turnover frequency (TOF) of 0.18 s^{-1} and a lower apparent activation energy of 51 kJ mol^{-1} in comparison to the catalyst with low silanol sites (0.06 s^{-1} and 101 kJ mol^{-1}). The optimal catalyst with 0.48 wt% Pd showed 78% CO conversion and 96% DMO+DMC selectivity, and excellent stability during the continuous test of 200 h. It was found that the catalytic performance strongly depended on the catalyst activation, as the heat treatment could tune the silanols around the Pd species on the S-1 zeolite. Furthermore, the existence of synergistic interactions between silanols and Pd was

confirmed by a series of in situ infrared experiments, and the enhanced interactions could improve the adsorption of CO reactant on the Pd species. Finally, the newly designed Pd/S-1 catalyst with high activity on the co-synthesis of DMO and DMC by understanding the Pd-silanol synergistic interactions was reported.

Declaration of Competing Interest

The authors declare no competing financial interest.

Acknowledgements

This project was supported by the National Key Research and Development Program of China (2022YFE0116000), National Natural Science Foundation of China (21908246, 21975285 and 22175200), Recruitment Program of High-end Foreign Experts (G2022152005L) and Sino-French International Research Network (IRN) "Zeolites". The authors would like to thank Kehui Han from Shiyanjia Lab (www.shiyanjia.com) for the characterization of aberration-corrected HAADF-STEM.

References

[1] Z. Li, S. Ji, Y. Liu, X. Cao, S. Tian, Y. Chen, Z. Niu, Y. Li, Well-defined materials for heterogeneous catalysis: From nanoparticles to isolated single-atom sites. Chem. Rev. 120 (2020) 623–682.

[2] A. Parastaev, V. Muravev, E. Huertas Osta, A.J.F. van Hoof, T.F. Kimpel, N. Kosinov, E.J.M. Hensen, Boosting CO_2 hydrogenation via size-dependent metal-support interactions in cobalt/ceria-based catalysts. Nat. Catal. 3 (2020) 526–533.

[3] Z. Ren, Y. Cao, R. Cai, X. Dai, Y. Wei, F. Nie, X. Yin, Y. Gan, B. Wu, Y. Ye, X. Huang, Metal-support interaction modulate the sulfidation and dispersion of MoS_2

slabs on hierarchical KNiMo|ZnCrAl-based multifunctional catalysts for selective conversion of syngas to higher alcohols, Chem. Eng. J. 440 (2022) 135831.

[4] P. Wu, S. Tan, J. Moon, Z. Yan, V. Fung, N. Li, S. Yang, Y. Cheng, C.W. Abney, Z. Wu, A. Savara, A.M. Momen, D. Jiang, D. Su, H. Li, W. Zhu, S. Dai, H. Zhu, Harnessing strong metal-support interactions via a reverse route. Nat. Commun. 11 (2020) 3042.

[5] M. Wang, B. Zhao, C. Cheng, F. Chen, M. Sun, Y. Shi, B. Zhang, Boosting CO_2-to-CO selectivity and durability by metal-support interaction and encapsulated effect of Ni@C capsules, Chem. Eng. J. 454 (2023) 140000.

[6] Q.F. Lin, Z.R. Gao, C. Lin, S. Zhang, J. Chen, Z. Li, X. Liu, W. Fan, J. Li, X. Chen, M.A. Camblor, F.J. Chen, A stable aluminosilicate zeolite with intersecting three-dimensional extra-large pores. Science 374 (2021) 1605–1608.

[7] Y. Chai, S. Liu, Z. Zhao, J. Gong, W. Dai, G. Wu, N. Guan, L. Li, Selectivity modulation of encapsulated palladium nanoparticles by zeolite microenvironment for biomass catalytic upgrading. ACS Catal. 8 (2018) 8578–8589.

[8] I.C. Medeiros-Costa, E. Dib, N. Nesterenko, J.P. Dath, J.P. Gilson, S. Mintova, Silanol defect engineering and healing in zeolites: Opportunities to fine-tune their properties and performances. Chem. Soc. Rev. 50 (2021) 11156–11179.

[9] J. Xu, R. Wang, Y. Zhang, L. Li, W. Yan, J. Wang, G. Liu, X. Su, Y. Huang, T. Zhang, Identification of the structure of Ni active sites for ethylene oligomerization on an amorphous silica-alumina supported nickel catalyst. Chin. J. Catal. 42 (2021) 2181–2188.

[10] P. Wu, J. Ruan, L. Wang, L. Wu, Y. Wang, Y. Liu, W. Fan, M. He, O. Terasaki, T. Tatsumi, Methodology for synthesizing crystalline metallosilicates with expanded pore windows through molecular alkoxysilylation of zeolitic lamellar precursors. J. Am. Chem. Soc. 130 (2008) 8178–8187.

[11] M. Choi, H.S. Cho, R. Srivastava, C. Venkatesan, D.H. Choi, R. Ryoo, Amphiphilic organosilane-directed synthesis of crystalline zeolite with tunable

mesoporosity. Nat. Mater. 5 (2006) 718–723.

[12] J. Grand, S.N. Talapaneni, A. Vicente, C. Fernandez, E. Dib, H.A. Aleksandrov, G.N. Vayssilov, R. Retoux, P. Boullay, J. Gilson, V. Valtchev, S. Mintova, One-pot synthesis of silanol-free nanosized MFI zeolite. Nat. Mater. 16 (2017) 1010–1015.

[13] S.V. Konnov, F. Dubray, E.B. Clatworthy, C. Kouvatas, J.P. Gilson, J.P. Dath, D. Minoux, C. Aquino, V. Valtchev, S. Moldovan, S. Koneti, N. Nesterenko, S. Mintova, Novel strategy for the synthesis of ultra-stable single-site Mo-ZSM-5 zeolite nanocrystals. Angew. Chem. Int. Ed. 59 (2020) 19553–19560.

[14] G. Feng, P. Cheng, W. Yan, M. Boronat, X. Li, J.H. Su, J. Wang, Y. Li, A. Corma, R. Xu, J. Yu, Accelerated crystallization of zeolites via hydroxyl free radicals. Science 351 (2016) 1188–1191.

[15] D. Zhao, X. Tian, D.E. Doronkin, S. Han, V.A. Kondratenko, J. Grunwaldt, A. Perechodjuk, T.H. Vuong, J. Rabeah, R. Eckelt, U. Rodemerck, D. Linke, G. Jiang, H. Jiao, E.V. Kondratenko, In situ formation of ZnO_x species for efficient propane dehydrogenation. Nature 599 (2021) 234–238.

[16] L. Qi, M. Babucci, Y. Zhang, A. Lund, L. Liu, J. Li, Y. Chen, A.S. Hoffman, S.R. Bare, Y. Han, B.C. Gates, A.T. Bell, Propane dehydrogenation catalyzed by isolated Pt atoms in ≡SiOZn-OH nests in dealuminated zeolite beta. J. Am. Chem. Soc. 143 (2021) 21364–21378.

[17] T. Li, F. Krumeich, J. Ihli, Z. Ma, T. Ishikawa, A.B. Pinar, J.A. van Bokhoven, Heavy atom labeling enables silanol defect visualization in silicalite-1 crystals. Chem. Commun. 55 (2019) 482–485.

[18] Q. Zhang, J. Yu, A. Corma, Applications of zeolites to C1 chemistry: recent advances, challenges, and opportunities. Adv. Mater. 32 (2020) 2002927.

[19] W. Zhou, K. Cheng, J. Kang, C. Zhou, V. Subramanian, Q. Zhang, Y. Wang, New horizon in C1 chemistry: Breaking the selectivity limitation in transformation of syngas and hydrogenation of CO_2 into hydrocarbon chemicals

and fuels. Chem. Soc. Rev. 48 (2019) 3193–3228.

[20] C. Wang, L. Han, P. Chen, G. Zhao, Y. Liu, Y. Lu, High-performance, low Pd-loading microfibrous-structured Al-fiber@ns-AlOOH@Pd catalyst for CO coupling to dimethyl oxalate. J. Catal. 337 (2016) 145–156.

[21] C. Wang, Y. Jia, Z. Zhang, G. Zhao, Y. Liu, Y. Lu, Role of PdC_x species in $Pd@PdC_x$/AlOOH/Al-fiber catalyst for the CO oxidative coupling to dimethyl oxalate. Appl. Surf. Sci. 478 (2019) 840–845.

[22] P. Kumar, V.C. Srivastava, U.L. Štangar, B. Mušič, I.M. Mishra, Y. Meng, Recent progress in dimethyl carbonate synthesis using different feedstock and techniques in the presence of heterogeneous catalysts. Catal. Rev. 63 (2021) 363–421.

[23] S. Huang, B. Yan, S. Wang, X. Ma, Recent advances in dialkyl carbonates synthesis and applications. Chem. Soc. Rev. 44 (2015) 3079–3116.

[24] W. Kuan, W. Yu, F. Tu, C. Chung, Y. Chang, M.M. Lin, T. Yu, L. Chen, Facile reflux preparation of defective mesoporous ceria nanorod with superior catalytic activity for direct carbon dioxide conversion into dimethyl carbonate, Chem. Eng. J. 430 (2022) 132941.

[25] H. Yue, X. Ma, J. Gong, An alternative synthetic approach for efficient catalytic conversion of syngas to ethanol. Acc. Chem. Res. 47 (2014) 1483–1492.

[26] H. Tan, Z. Chen, K. Jing, J. Sun, Y. Xu, N. Zhang, Z. Xu, G. Guo, Paired-Pd(II) centers embedded in HKUST-1 framework: Tuning the selectivity from dimethyl carbonate to dimethyl oxalate. J. Energy Chem. 67 (2022) 233–240.

[27] Z. Wang, J. Sun, Z. Xu, G. Guo, CO direct esterification to dimethyl oxalate and dimethyl carbonate: The key functional motifs for catalytic selectivity. Nanoscale 12 (2020) 20131–20140.

[28] C. Wang, J. Ding, G. Zhao, T. Deng, Y. Liu, Y. Lu, Microfibrous-structured Pd/AlOOH/Al-fiber for CO coupling to dimethyl oxalate: Effect of morphology of AlOOH nanosheet endogenously grown on Al-fiber. ACS Appl. Mater. Interfaces

9 (2017) 9795–9804.

[29] X. Gao, Y. Zhao, S. Wang, Y. Yin, B. Wang, X. Ma, A Pd-Fe/α-Al_2O_3/cordierite monolithic catalyst for CO coupling to oxalate. Chem. Eng. Sci. 66 (2011) 3513–3522.

[30] S. Peng, Z. Xu, Q. Chen, Z. Wang, D. Lv, J. Sun, Y. Chen, G. Guo, Enhanced stability of Pd/ZnO catalyst for CO oxidative coupling to dimethyl oxalate: Effect of Mg. ACS Catal. 5 (2015) 4410–4417.

[31] H. Tan, Y. Xu, S. Rong, R. Zhao, H. Cui, Z. Chen, Z. Xu, N. Zhang, G. Guo, Enhanced metal-support interaction between Pd and hierarchical Nb_2O_5 via oxygen defect induction to promote CO oxidative coupling to dimethyl oxalate. Nanoscale 13 (2021) 18773–18779.

[32] K. Jing, Y. Fu, Z. Chen, T. Zhang, J. Sun, Z. Xu, G. Guo, Boosting interfacial electron transfer between Pd and ZnTi-LDH via defect induction for enhanced metal-support interaction in CO direct esterification reaction. ACS Appl. Mater. Inter. 13 (2021) 24856–24864.

[33] C. Wang, W. Xu, Z. Qin, X. Liu, S. Mintova, Low-temperature synthesis of α-alumina nanosheets on microfibrous-structured Al-fibers for Pd-catalyzed CO oxidative coupling to dimethyl oxalate. Catal. Today 354 (2020) 158–166.

[34] U. Romano, R. Tesel, G. Cipriani, L. Micucci, Method for the preparation of esters of carbonic acid. US Patent 4,218,391 (1980).

[35] G. Paret, G. Donati, M. Ghirardini, Process for producing dimethyl carbonate and apparatus suitable for such purpose. US Patent 5,536,864 (1996).

[36] N. Keller, G. Rebmann, V. Keller, Catalysts, mechanisms and industrial processes for the dimethylcarbonate synthesis. J. Mol. Catal. A: Chem. 317 (2010) 1–18.

[37] S. Uchiumi, K. Ataka, T. Matsuzaki, Oxidative reactions by a palladium-alkyl nitrite system. J. Organomet. Chem. 576 (1999) 279–289.

[38] X. Gao, X. Ma, S. Wang, Z. Li, Catalytic performance of $PdCl_2$-$CuCl_2$/Li-Al-O

for synthesis of diethyl carbonate from CO and ethyl nitrite at low pressure. Chin. J. Catal. 28 (2007) 720−724.

[39] H. Tan, Z. Chen, Z. Xu, J. Sun, Z. Wang, R. Si, W. Zhuang, G. Guo, Synthesis of high-performance and high-stability Pd(II)/NaY catalyst for CO direct selective conversion to dimethyl carbonate by rational design. ACS Catal. 9 (2019) 3595−3603.

[40] C. Wang, N. Xu, T. Liu, W. Xu, H. Guo, Y. Li, P. Bai, X. Wu, X. Gong, X. Liu, S. Mintova, Mechanical pressure-mediated Pd active sites formation in NaY zeolite catalysts for indirect oxidative carbonylation of methanol to dimethyl carbonate. J. Catal. 396 (2021) 269−280.

[41] Y. Yamamoto, T. Matsuzaki, S. Tanaka, K. Nishihira, K. Ohdan, A. Nakamura, Y. Okamoto, Catalysis and characterization of Pd/NaY for dimethyl carbonate synthesis from methyl nitrite and CO. J. Chem. Soc. Faraday Trans. 93 (1997) 3721−3727.

[42] Y. Xu, Z. Wang, H. Tan, K. Jing, Z. Xu, G. Guo, Lewis acid sites in MOFs supports promoting the catalytic activity and selectivity for CO esterification to dimethyl carbonate. Catal. Sci. Technol. 10 (2020) 1699−1707.

[43] D. Wang, J. Liu, X. Cheng, X. Kang, A. Wu, C. Tian, H. Fu, Trace Pt clusters dispersed on SAPO-11 promoting the synergy of metal sites with acid sites for high-effective hydroisomerization of n-Alkanes. Small Methods 3 (2019) 1800510.

[44] Z. Li, W. Wang, D. Yin, J. Lv, X. Ma, Effect of alkyl nitrite decomposition on catalytic performance of CO coupling reaction over supported palladium catalyst. Front. Chem. Sci. Eng. 6 (2012) 410−414.

[45] Z. Mao, C.T. Campbell, Apparent activation energies in complex reaction mechanisms: A simple relationship via degrees of rate control. ACS Catal. 9 (2019) 9465−9473.

[46] H. Guan, J. Lin, L. Li, X. Wang, T. Zhang, Highly active subnano Rh/Fe$(OH)_x$

catalyst for preferential oxidation of CO in H_2-rich stream. Appl. Catal. B 184 (2016) 299–308.

[47] G. Kyriakou, C.R. Theocharis, The anomalous sorptive behaviour of ZSM-5 and silicalite-1: Observation of low-pressure hysteresis in nitrogen adsorption. Stud. Surf. Sci. Catal. 144 (2002) 709–716.

[48] M. Li, Y. Zhou, Y. Fang, Functioned carbon nanotube templated hierarchical silicate-1 synthesis: On the existence of super-micropore. Microporous Mesoporous Mater. 225 (2016) 392–398.

[49] N. Lempesis, N. Smatsi, V.G. Mavrantzas, S.E. Pratsinis, Pressure- and temperature-induced monoclinic-to-orthorhombic phase transition in silicalite-1. J. Phys. Chem. C 122 (2018) 6217–6229.

[50] E. Rodeghero, A. Martucci, G. Cruciani, R. Bagatin, E. Sarti, V. Bosi, L. Pasti, Kinetics and dynamic behaviour of toluene desorption from ZSM-5 using in situ high-temperature synchrotron powder X-ray diffraction and chromatographic techniques. Catal. Today 277 (2016) 118–125.

[51] Z. Yang, H. Li, H. Zhou, L. Wang, L. Wang, Q. Zhu, J. Xiao, X. Meng, J. Chen, F. Xiao, Coking-resistant iron catalyst in ethane dehydrogenation achieved through siliceous zeolite modulation. J. Am. Chem. Soc. 142 (2020) 16429–16436.

[52] C. Wang, W. Xu, Z. Qin, H. Guo, X. Liu, S. Mintova, Highly active Pd containing EMT zeolite catalyst for indirect oxidative carbonylation of methanol to dimethyl carbonate. J. Energy Chem. 52 (2021) 191–201.

[53] A.F. Lee, J.N. Naughton, Z. Liu, K. Wilson, High-pressure XPS of crotyl alcohol selective oxidation over metallic and oxidized Pd(111). ACS Catal. 2 (2012) 2235–2241.

[54] S.P. Chenakin, G. Melaet, R. Szukiewicz, N. Kruse, XPS study of the surface chemical state of a Pd/(SiO_2+TiO_2) catalyst after methane oxidation and SO_2 treatment. J. Catal. 312 (2014) 1–11.

[55] Y. Dong, S. Huang, S. Wang, Y. Zhao, J. Gong, X. Ma, Synthesis of dimethyl carbonate through vapor-phase carbonylation catalyzed by Pd-doped zeolites: Interaction of Lewis acidic sites and Pd species. ChemCatChem 5 (2013) 2174–2177.

[56] G. Vilé, D. Albani, M. Nachtegaal, Z. Chen, D. Dontsova, M. Antonietti, N. López, J. Pérez-Ramírez, A stable single-site palladium catalyst for hydrogenations. Angew. Chem. Int. Ed. 54 (2015) 11265−11269.

[57] K. Khivantsev, N.R. Jaegers, L. Kovarik, J.C. Hanson, F.F. Tao, Y. Tang, X. Zhang, I.Z. Koleva, H.A. Aleksandrov, G.N. Vayssilov, Y. Wang, F. Gao, J. Szanyi, Achieving atomic dispersion of highly loaded transition metals in small-pore zeolite SSZ-13: High-capacity and high-efficiency low-temperature CO and passive NO_x adsorbers. Angew. Chem. Int. Ed. 57 (2018) 16672−16677.

[58] C. Wang, P. Chen, Y. Li, G. Zhao, Y. Liu, Y. Lu, In situ DRIFTS study of CO coupling to dimethyl oxalate over structured Al-fiber@ns-AlOOH@Pd catalyst. J. Catal. 344 (2016) 173−183.

[59] B. Han, M. Dong, R. Zhang, L. Ling, M. Fan, P. Liu, B. Wang, CO oxidative coupling to dimethyl oxalate over Pd monolayer supported on SiC substrate: Insight into the effects of different exposed terminals. Mol. Catal. 515 (2021) 111926.

[60] S. Bordiga, P. Ugliengo, A. Damin, C. Lamberti, G. Spoto, A. Zecchina, G. Spanò, R. Buzzoni, L. Dalloro, F. Rivetti, Hydroxyls nests in defective silicalites and strained structures derived upon dehydroxylation: Vibrational properties and theoretical modelling. Top. Catal. 15 (2001) 43–52.

[61] M.E. Dose, K. Zhang, J.A. Thompson, J. Leisen, R.R. Chance, W.J. Koros, B.A. McCool, R.P. Lively, Effect of crystal size on framework defects and water uptake in fluoride mediated silicalite-1. Chem. Mater. 26 (2014) 4368−4376.

[62] I. Grosskreuz, H. Gies, B. Marler, Alteration and curing of framework defects by heating different as-made silica zeolites of the MFI framework type. Microporous

Mesoporous Mater. 291 (2020) 109683.

[63] F. Dubray, S. Moldovan, C. Kouvatas, J. Grand, C. Aquino, N. Barrier, J. Gilson, N. Nesterenko, D. Minoux, S. Mintova, Direct evidence for single molybdenum atoms incorporated in the framework of MFI zeolite nanocrystals. J. Am. Chem. Soc. 141 (2019) 8689−8693.

[64] K. Hadjiivanov, Identification and characterization of surface hydroxyl groups by infrared spectroscopy. Adv. Catal. 57 (2014) 99−318.

[65] M. Westgård Erichsen, S. Svelle, U. Olsbye, The influence of catalyst acid strength on the methanol to hydrocarbons (MTH) reaction. Catal. Today 215 (2013) 216−223.

[66] T. Montanari, L. Castoldi, L. Lietti, G. Busca, Basic catalysis and catalysis assisted by basicity: FT-IR and TPD characterization of potassium-doped alumina. Appl. Catal. A 400 (2011) 61−69.

[67] A. Paredes-Nunez, I. Jbir, D. Bianchi, F.C. Meunier, Spectrum baseline artefacts and correction of gas-phase species signal during diffuse reflectance FT-IR analyses of catalysts at variable temperatures. Appl. Catal. A 495 (2015) 17−22.

[68] J. Sirita, S. Phanichphant, F.C. Meunier, Quantitative analysis of adsorbate concentrations by diffuse reflectance FT-IR. Anal. Chem. 79 (2007) 3912−3918.